

Enhancing Ground Penetrating Radar (GPR) Data Analysis Utilizing Machine Learning

Mohanad Abd Shehab^{1*} , Musab T.S. Al-Kaltakchi¹ , Ammar Dukhan¹ , Wai Lok Woo² 

¹Electrical Engineering Department, College of Engineering, Mustansiriyah University, Baghdad, Iraq

²Department of Computer and Information Sciences, Northumbria University, Newcastle upon Tyne NE1 8ST, UK

*Email: mohanadshehab@uomustansiriyah.edu.iq

Article Info	Abstract
<p>Received 18/03/2024</p> <p>Revised 28/12/2024</p> <p>Accepted 02/02/2025</p>	<p>Ground Penetrating Radar is a non-destructive geophysical technique that utilizes radio waves to generate images of the Earth's subsurface to point out the location of buried evidence. In this paper, it is used to identify structures and types of seismic images of a real oil and gas field. This work employs GPR with 500MHz to permit the EMW to penetrate deep and to provide a good resolution for images generated. Gray-Level Co-Occurrence Matrix and Wavelet feature extractor approaches are mixed to extract 48 selected features. Subsequently, preprocessing techniques are utilized to improve GPR data analysis and interpretation, including refining data, imputing the missing values, normalizing all data, and splitting them into 70% for the training and 30% for the testing phases. Finally, various machine learning techniques are employed to classify the collected images using models like Decision Trees,agged trees, Naive Bayes, Artificial Neural Networks, Quadratic Discriminant Analysis, Support Vector Machines, and K-nearest neighbors. The performance metrics of all the machine learning approaches are worthy, and the proposed KNN can achieve an accuracy of 98.169%, 14 seconds of training time, and less than a few seconds of testing time.</p>

Keywords: Accuracy; Classifiers; Ground Penetrating Radar; Seismic Images; Real Oil and Gas Field

1. Introduction

Ground Penetrating Radar (GPR) is an electromagnetic subsurface device used in engineering for subsurface structure identification and non-destructive testing with a wide range of uses [1]. It exploits the characteristics of radar waves to determine geological material features [2]. Moreover, the nature of non-destructive, which works within the microwave radio band of GPR, makes a difference in distinguishing various materials [3] and offers high-resolution and near-surface bits of knowledge [4]. However, flag weakening in a few soil conditions confines entrance profundity [5]. Lower frequencies, such as 100 MHz or lower, can penetrate deeper into the ground but may have lower resolution. Higher frequencies, such as 1 GHz or higher, provide higher resolution but penetrate less deeply, so the seismic GPR utilizes moderate frequency Electromagnetic (EM) waves for subsurface imaging to attain the advantages of both [6]-[8]. Using pulsed EMW with frequencies between 1 and 4000 MHz, GPR technology records the time for waves reflected from subsurface contacts to reach the surface. Equation (1) can be used to find an interface's depth (D):

$$D = v \cdot t / 2 \quad (1)$$

Where D is the depth of the reflector (interface) beneath the surface, v is the velocity of the radar wave pulse as it travels through the subsurface material, and t is the two-way travel time of the pulsed radar wave.

The conductivity of the ground, governed mainly by variables like water content, salinity, temperature, density, and the frequency of the EMW employed, has a considerable impact on the effective penetration depth of radar probing [9]. Reflections occur at interfaces with variable dielectric constants rather than acoustic impedances, and this process is similar to reflection seismology [10]. However, GPR uses electromagnetic energy instead of acoustic energy. The electrical dielectric constants of soils and rocks have a major role in controlling the propagation of EM waves since most have extremely low conductivity, around 10^{-2} S/m. The propagation velocity (v) of radar signals is determined by the medium's relative dielectric constant (ϵ_r) and other factors. For most geological materials with relative permeability (μ_r) close to unity, radar velocity can be

approximated by equation (2), where C is the velocity of EMW in free space [11].

$$v = \frac{c}{(\mu_r \epsilon_r)^{1/2}} \approx \frac{c}{(\epsilon_r)^{1/2}} \quad (2)$$

Where $\mu_r = \mu/\mu_0$ is the relative permeability of the medium, which is about unity for most earth soils and rocks. $\epsilon_r = \epsilon/\epsilon_0$ is the ratio of the medium's dielectric permittivity to that of free space. Geological formations exhibit a wide range of dielectric constants, with dry sand/gravel, silt, unaltered hard rocks, permafrost soils, and ice having lower values (3-10). In contrast, water has a high value of 81. Water content significantly impacts electromagnetic wave attenuation, leading to the choice of high frequencies for shallow investigations and low frequencies for greater depths. The penetration depth is limited by ground conductivity, frequency, and radiated power. Seismic GPR utilizes seismic waves for subsurface imaging and is commonly employed in natural resource exploration, civil engineering projects, and geological work [12]. This work explores the GPR for identifying subsurface structures in a hydrocarbon oil and gas field. The study aims to enhance subsurface characterization, imaging, and classification accuracy and efficiency by employing a 500MHz GPR system, robust feature extraction methods, and various machine learning classifiers. The subsequent sections include Machine Learning with GPR, which discusses the application of machine learning techniques in GPR analysis; The proposed work, which specifies the methodology employed; Data Preprocessing and Feature Extraction, which describes the preprocessing steps and feature extraction methods; Results and Discussion, that are presenting and analyzing the experimental results; and finally Conclusion, which summarizes the key findings and future research directions.

2. Machine Learning with GPR

Machine Learning (ML) has become pivotal in analyzing GPR data due to its proficiency in feature extraction, automating tasks such as object identification, geological interface detection, and soil property estimation. ML algorithms excel at recognizing patterns and subsurface features, including buried infrastructure. ML improves the precision and speed of extracting properties like electrical conductivity and dielectric permittivity in an inversion, enabling detailed subsurface characterization. ML assists in material classification based on GPR signatures, facilitating the identification of soil types, geological layers, and subsurface features. Additionally, it supports data fusion, integrating GPR with other geophysical data sources for a thorough subsurface overview. The following literature reviews offer valuable insights for those exploring the combination of ML and GPR. A brand-new near-real-time ML modeling technique is created for GPR simulations [13].

The ML scheme uses detailed GPR transducer modeling in Finite-Difference Time-Domain (FDTD) simulations and PCA to identify reinforcing bars in concrete, accurately determining size, position, and material qualities using actual and synthetic data. A novel ML scheme for GPR is described to estimate the diameter of reinforcing bars in concrete frameworks using neural networks trained on synthetic data and random forest

regression. This single A-scan input methodology provides real-time data without complex setups or multi-sensor techniques [14]. Liu et al. [15] introduced a method for automatically detecting and locating rebars in GPR imagery and streamlining the manual interpretation process. This method employed a Single Shot Multibox Detector (SSD) trained on genuine GPR data and migration techniques. The Artificial Algorithm (AI) method proposed achieves a detection accuracy of 90.9%, completing computations swiftly in 0.47 seconds for a 300×300 pixel GPR image. Through laboratory experiments, it demonstrates depth estimation errors of less than 1.5 mm (5%) and lateral position errors of less than 0.7 cm, indicating its suitability for real-time operation with handheld GPR systems, providing practical depth estimation accuracy.

Smitha and Singh [16] introduced a new supervised ML approach for landmine identification. It highlighted two main contributions: firstly, a performance analysis that compares Support Vector Machines (SVM) and Artificial Neural Networks (ANN) classifiers based on three features (major axis, minor axis, and principal component analysis); and secondly, a novel method that suggests five texture features (mean, variance, kurtosis, skewness, and entropy). These classifiers were trained on datasets comprising GPR images with surrogate landmines collected in the lab. The experiments cover various depths and include surrogate mines as well as non-mines. The ANN classifier outperformed the SVM with an accuracy ranging from 85% to 90% for training data samples in three and five-feature analyses. When tested on unseen samples, the ANN consistently achieves 5% to 10% higher accuracy than the SVM classifier.

Xiang et al. [17] addressed integrating GPR data with Building Information Modeling (BIM) to incorporate embedded rebars. This challenging task involved linking GPR data to BIM using Faster Convolutional Neural Network (R-CNN). GPR-scanned components are given labels, resulting in labeled photos that are then integrated with other photographs to create a 3D model. These labels were identified faster by R-CNN, and the projection relationship between the pictures and the model facilitated the 3D model's localization of the scanned elements. Evaluation of two concrete buildings demonstrates the method's accuracy in translating GPR data of rebars into corresponding BIM elements, preserving their correct distributions. Interpreting GPR data remains challenging due to variable ground conditions. Recent advancements in computer vision, particularly ANNs and CNNs, have been applied to extract information from GPR images, enhancing data interpretation.

Amaral et al. [18] utilized computer vision and deep learning algorithms, including YOLO-V3, Viola-Jones, and AlexNet, to automate information extraction from GPR images. These automated detection algorithms transform GPR by quickly quantifying and locating buried targets, reducing the need for highly trained professionals to perform these tasks. Rasol et al. [19] reviewed using GPR as a non-destructive geophysical method for assessing road pavements. It emphasizes using ML and intelligent data analysis in early pavement inspection to optimize maintenance, reduce costs, and extend infrastructure lifespan. GPR's advantages, including cost-effectiveness and non-invasiveness, are highlighted. The review showcases

GPR's successful application in detecting various inner damages in road pavements, such as deboning, sinkholes, and moisture. Additionally, it explores the integration of GPR with complementary techniques for more comprehensive pavement inspection.

A novel approach for interpreting seismic reflection horizons was presented using ANN, offering speed, precision, and reduced subjectivity compared to manual or control-point methods [20]. Long Short-Term Memory (LSTM) architecture is used for training, and convolutional models are used to create synthetic data. The technique is resilient against different noise and may be used for a wide range of field seismic datasets. Testing was done on synthetic, field seismic, and 2- and 3-dimensional data. Its successful application to GPR data demonstrated its adaptability. The problem of distinguishing between reflected and diffracted wave fields in the processing of seismic and GPR data was examined in the work [21].

In this work, GPR with 500MHz is employed first to permit the EMW to penetrate deep and to provide high-resolution gathering data; the data is presented as seismic images, texture with gray-level co-occurrence matrix (GLCM), and wavelet transform (WT) are used to extract 48 total features. After that, preprocessing techniques are utilized to improve GPR data analysis and interpretation, including refining data, imputing the missing values, normalizing all data, and splitting them into 70% for the training and 30% for the testing phases. Finally, different in nature ML approaches, using models like Decision Trees (DT), Bagged Trees (BT), Naive Bayes (NB), Artificial Neural Networks (ANN), Quadratic Discriminant Analysis (QDA), Support Vector Machines (SVM), and K-Nearest Neighbors (KNN) are employed to classify the collected images.

3. The Proposed Work

Fig. 1 shows the framework of the proposed system that includes the preprocessing and seven methods of ML, while Fig. 2 focuses on the flowchart of training and testing models. Exploration for oil and gas benefits greatly from using seismic data as it sheds light on subsurface geological formations. Seismic data is yielded for a real oil and gas field [22] to pinpoint possible hydrocarbon reserves and maximize well drilling locations. With specialized equipment, waves are sent into the Earth's subsurface, and their reflections are recorded for examination to collect this data. Seismic data is frequently separated into subgroups according to location, depth, or other criteria to make analysis easier. This work will employ a range of machine-learning techniques to distinguish between the various kinds of soil in a real hydrocarbon oil and gas field to enhance our comprehension of the geological aspects of this area [23]-[26]. The "seis_fan" subset refers to seismic data collected for two types of fan-shaped sediment deposits, as shown in Figs. 3-a and 3-b, while the "seis_road" subset refers to data collected for three types along a road or highway that runs through the field as depicted in Figs. 4-a, 4-b, and 4-c. As depicted in Figs, the "seis_emerson" subset refers to data collected for three types from a specific well or borehole in the field: 5-a, 5-b, 5-c, 5-d, and 5-e. A large number of seismic

samples, each lasting 0.001 seconds and covering a distance of 250 meters, are collected to create the dataset [22]. 10,010 instances make up this set, with 48 characteristics per instance and one column devoted to targets or classes. With a training-to-testing ratio of 70% to 30%, 7,007 occurrences of 48 features for training data and 3,003 instances for testing are produced. For assessment, a 10-fold cross-validation strategy is applied.

4. Data Preprocessing and Feature Extraction

Our dataset frequently faces missing data, which calls for an imputation approach to estimate and fill these gaps. One popular method in this area is imputation using the KNN algorithm. The KNN imputation technique replaces missing values in the dataset with estimated values that come from their closest neighbors as the following steps [27], [28]:

Identify Missing Values: Let $X = [x_{ij}]$ be the data matrix with m samples and n features. Identify the indices of missing values in X .

Calculate Distances: For each instance x_i with a missing value x_{ij} , calculate the Euclidean distance to all other instances x_p , using the not missing features Q only as in equation (3):

$$d(x_i, x_p) = \sum_{q \in Q} (x_{iq} - x_{ip})^2 \quad (3)$$

Find Nearest Neighbors: Select the k instances with the smallest distances to x_i .

Impute Missing Values: For each missing value x_{ij} , impute using the weighted mean of the k nearest neighbors as in equation (4):

$$x_{ij} = \frac{\sum \frac{x_{pj}}{d(x_i, x_p)}}{\sum \frac{1}{d(x_i, x_p)}} \quad (4)$$

The input data is also normalized using min-max to scale the features to a range [0, 1], as shown in equation (5):

$$x'_{ij} = \frac{x_{ij} - \min(x_j)}{\max(x_j) - \min(x_j)} \quad (5)$$

This guarantees that each feature receives the same attention, increases convergence, and strengthens the models' stability and interpretability.

Gray-Level Co-Occurrence Matrix (GLCM) [29] and Wavelet Transform (WT) [30] are two powerful techniques for feature extraction in image processing. GLCM captures texture information by considering the spatial relationship between pixel pairs, while WT decomposes an image into different frequency components, capturing frequency information. GLCM features include contrast, correlation, energy, homogeneity, and more [29], while WT features include mean, standard deviation, and entropy of the approximation and detail coefficients [30].

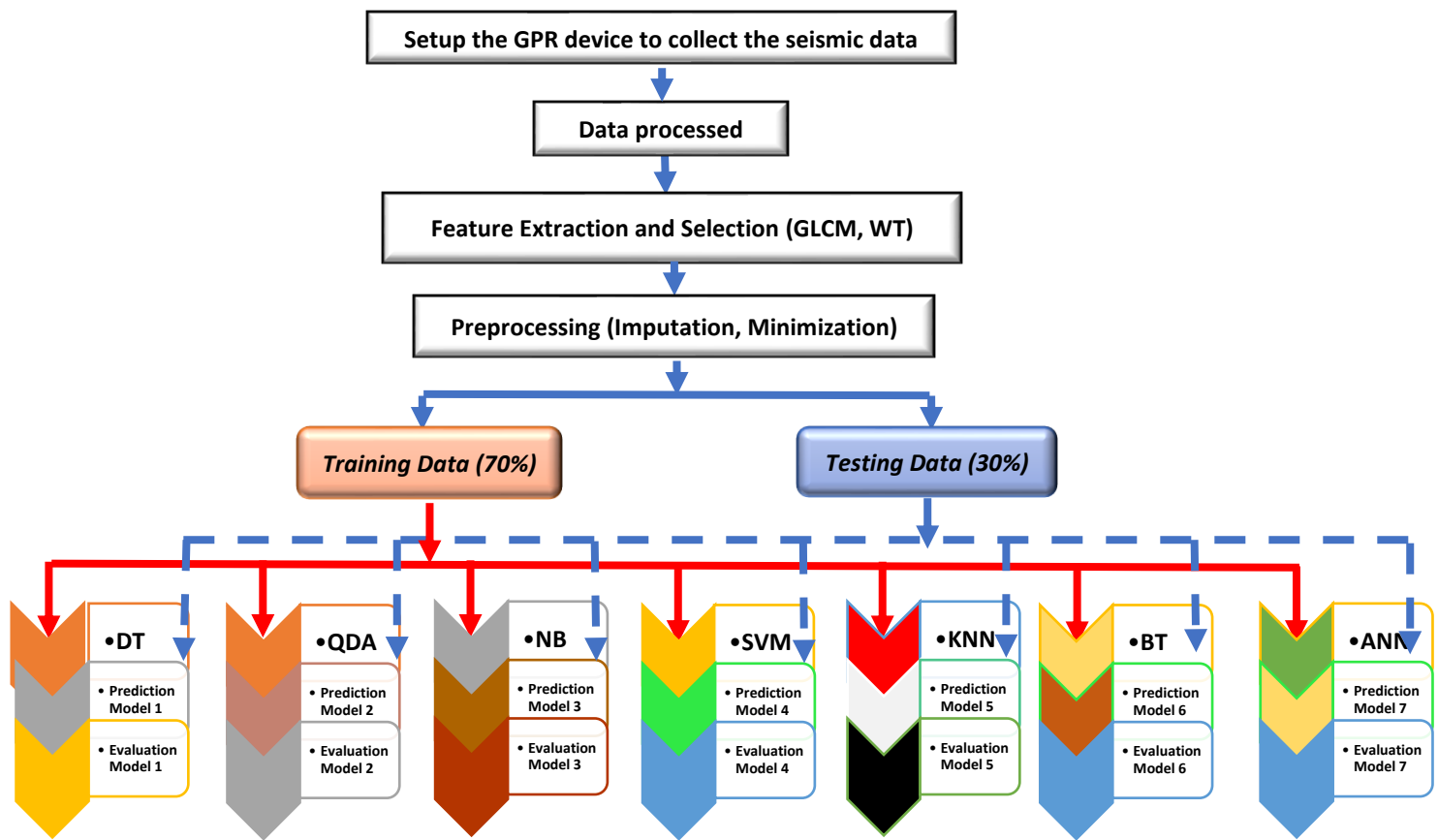


Figure 1. The framework of the proposed ML methods

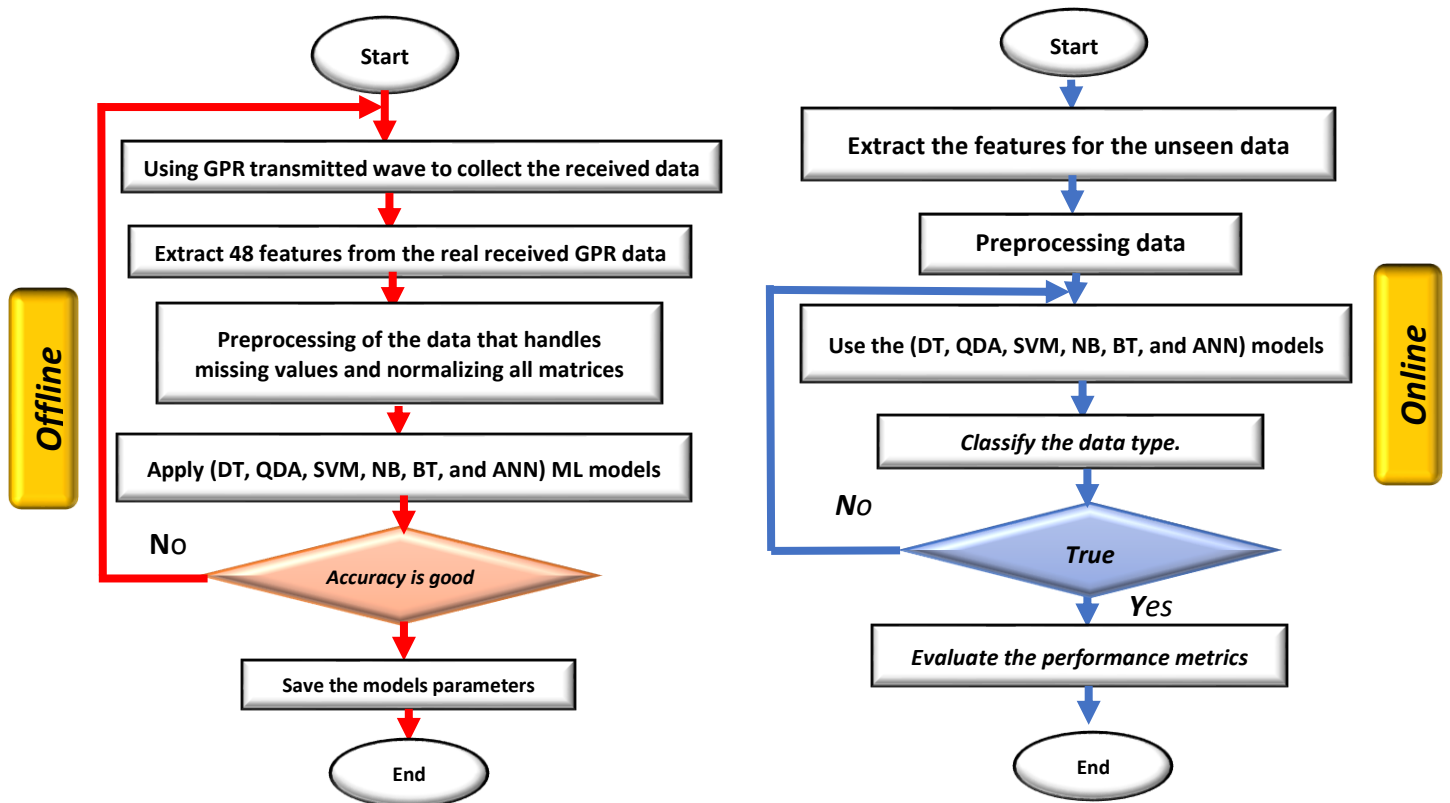
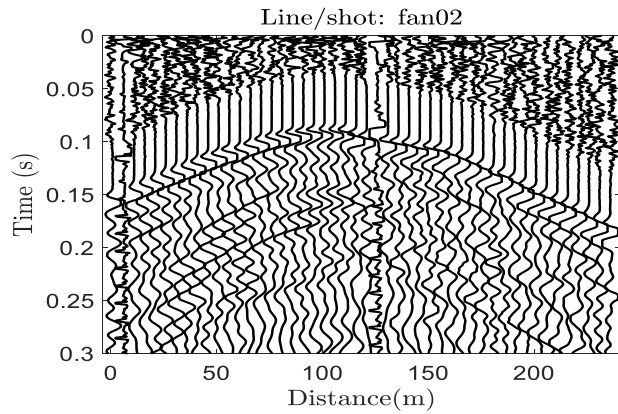
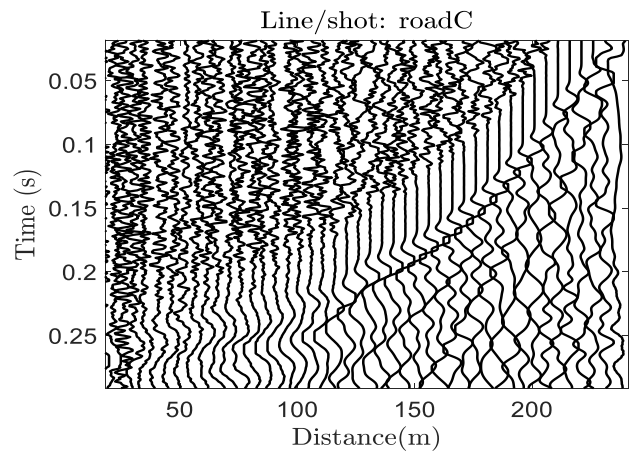
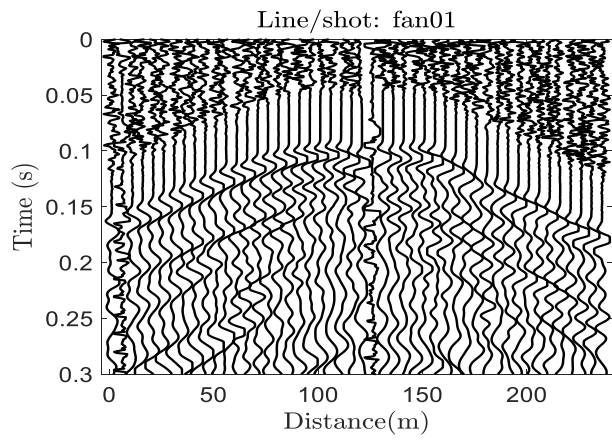


Figure 2. The flowchart of the offline and online models



Figures 4. a: seis_road 03, b: seis_road 04 & c: seis_road 05 seismic data

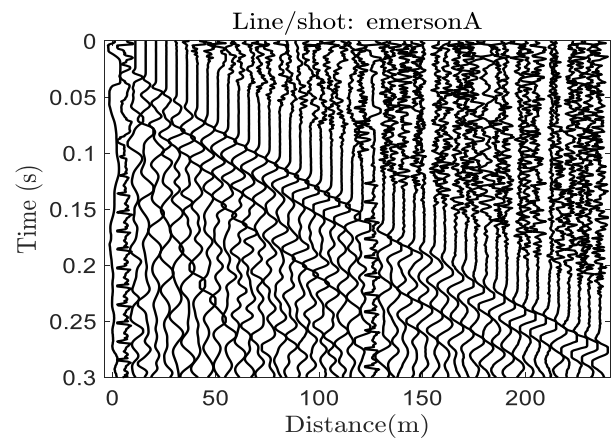
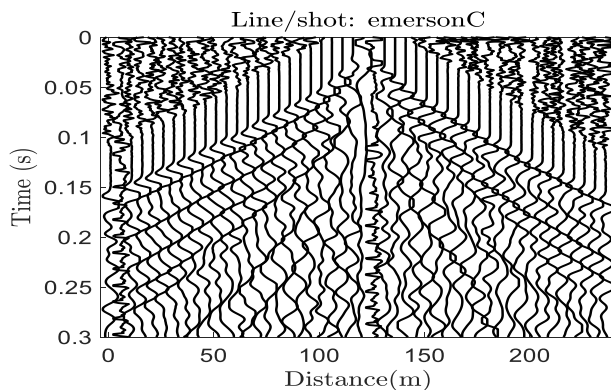
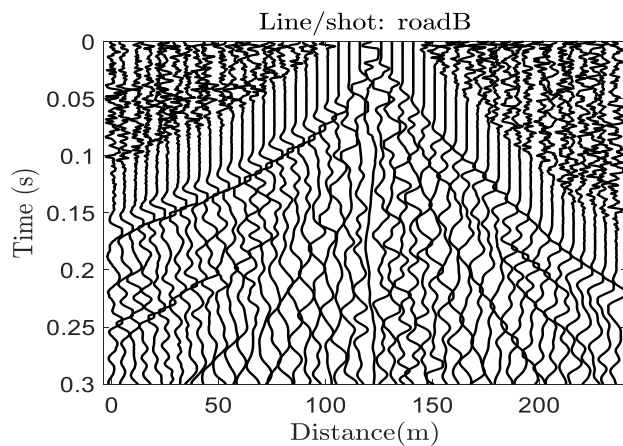
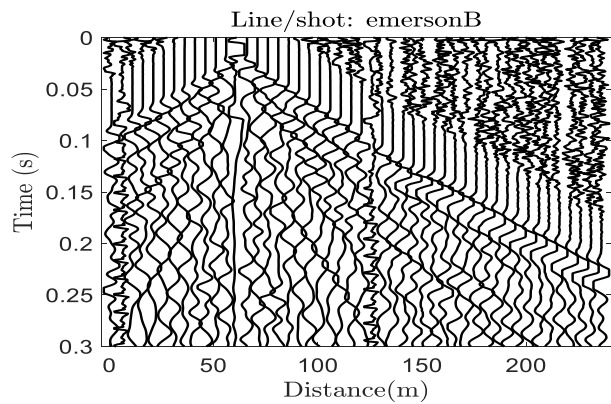
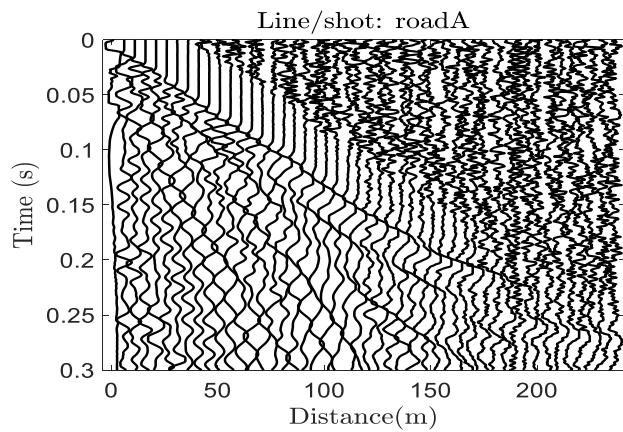
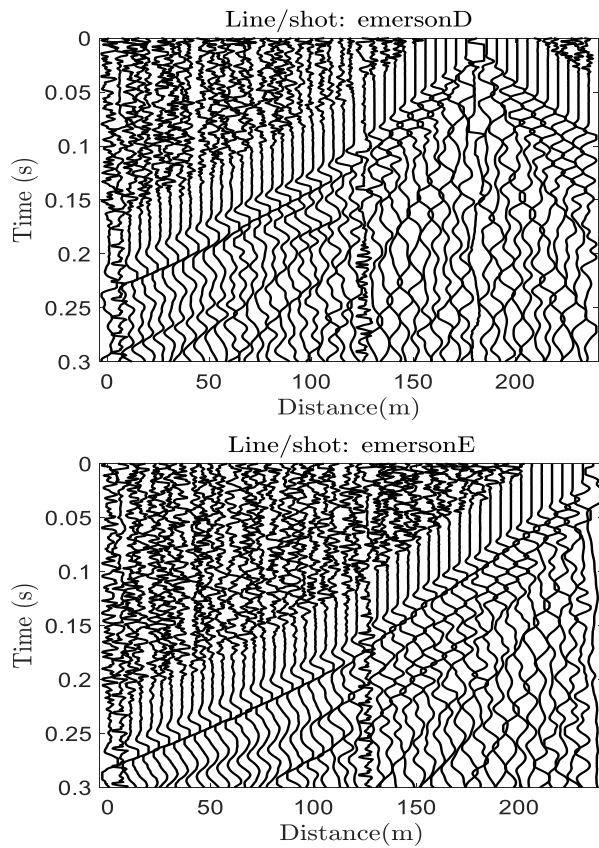


Figure 3. a: seis_fan01 & b: seis_fan02 seismic data





Figures 5. a, b, c, d, and e seis_ Emerson a to seis_ emerson e seismic data

5. Results and Discussion

The MATLAB software environment version 2021b is now being used to create all of the models for the GPR system and several machine learning techniques. Figs. 6 to 12 show training and testing confusion matrices for the seven models, with performance metrics like training accuracy, training duration, and testing accuracy explained in Table 1.

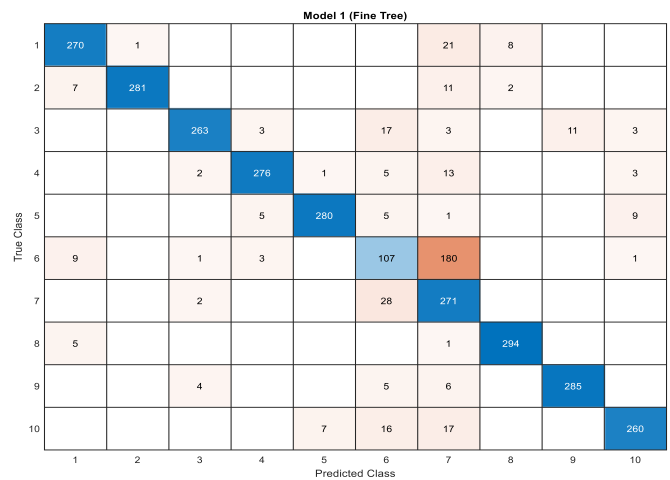
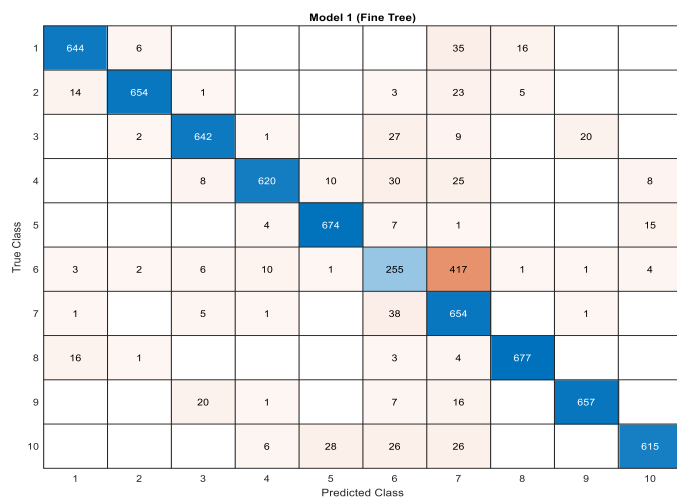


Figure 6. The confusion matrix for the DT classifier during the training and testing phases.

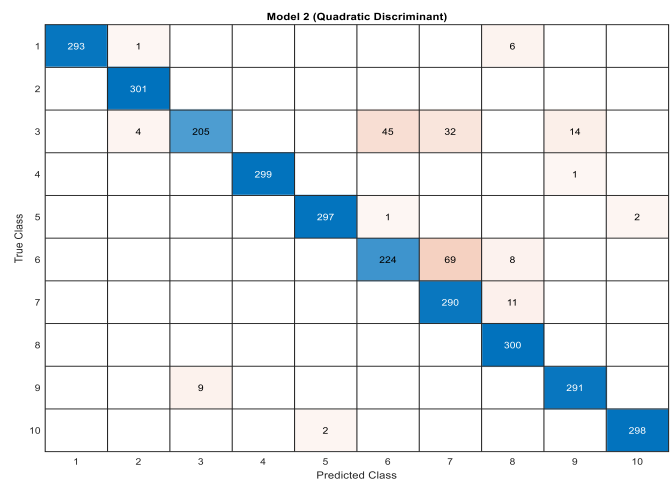
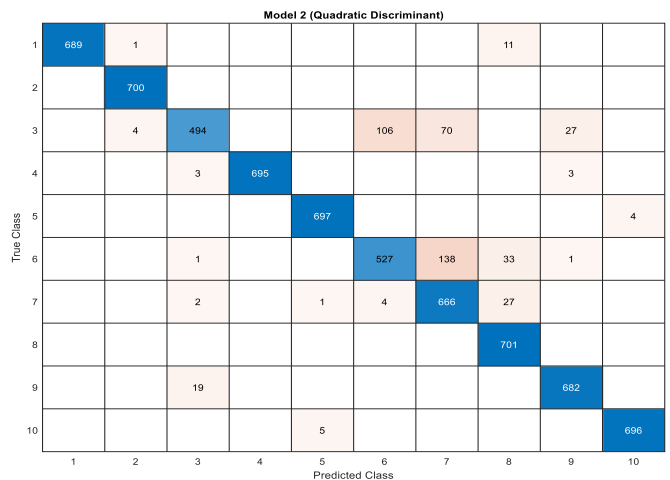


Figure 7. The confusion matrix for the QDA classifier during the training and testing phases.

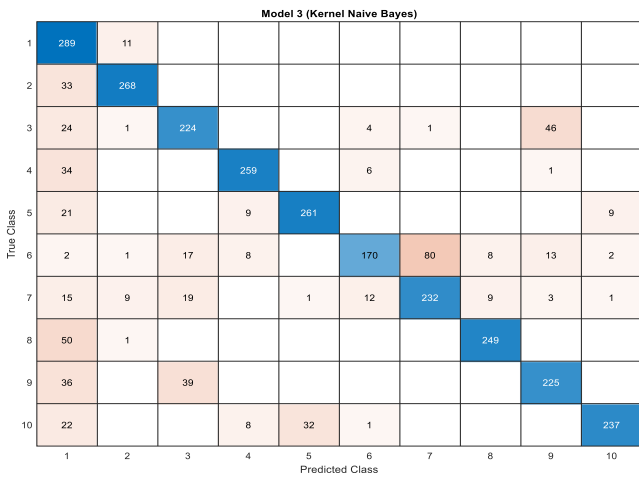
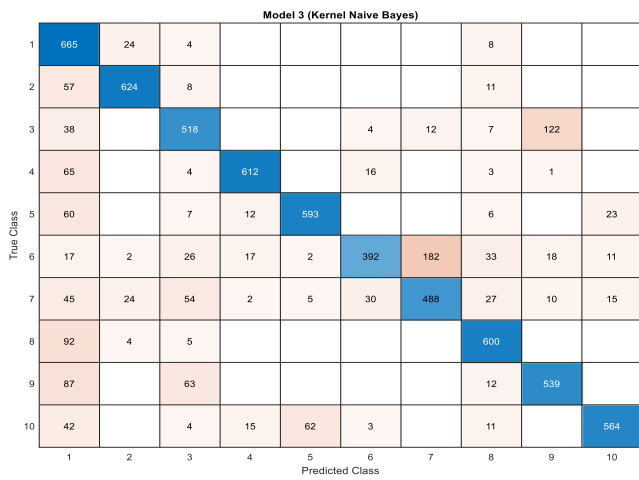


Figure 8. The confusion matrix for the NB classifier during the training and testing phases.

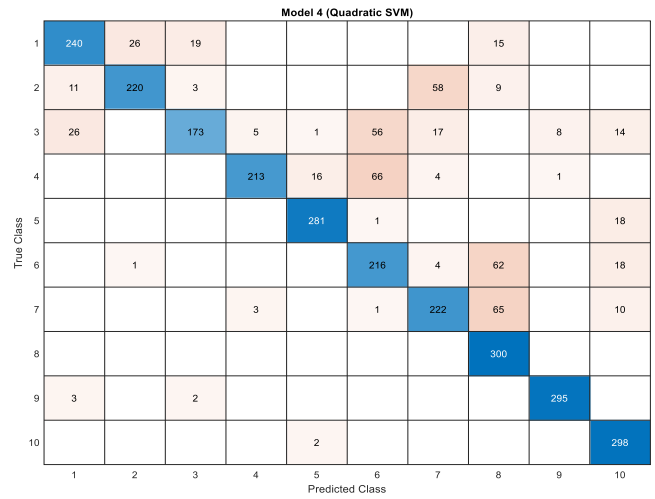
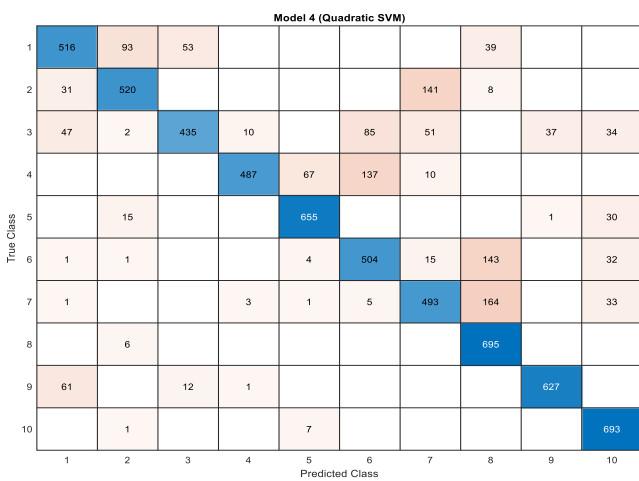


Figure 9. The confusion matrix for the SVM classifier during the training and testing phases.

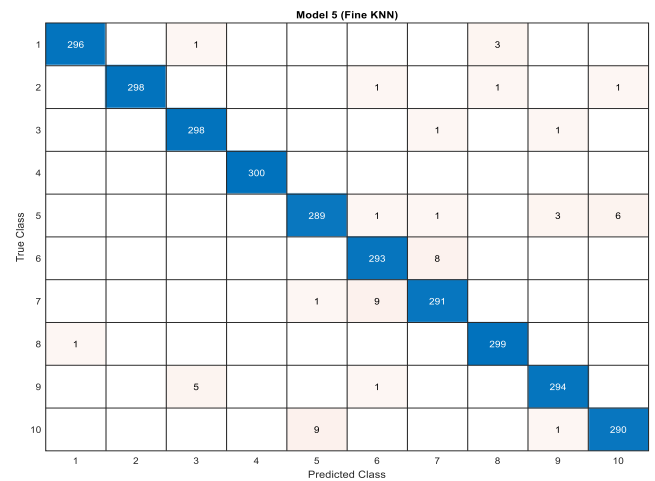
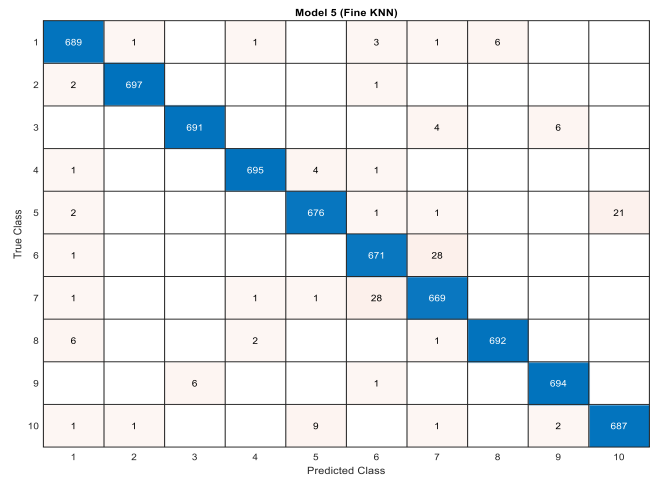


Figure 10. The confusion matrix for the KNN classifier during the training and testing phases.

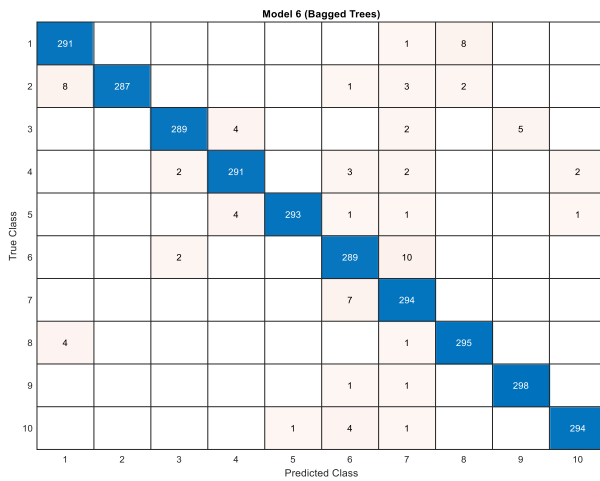
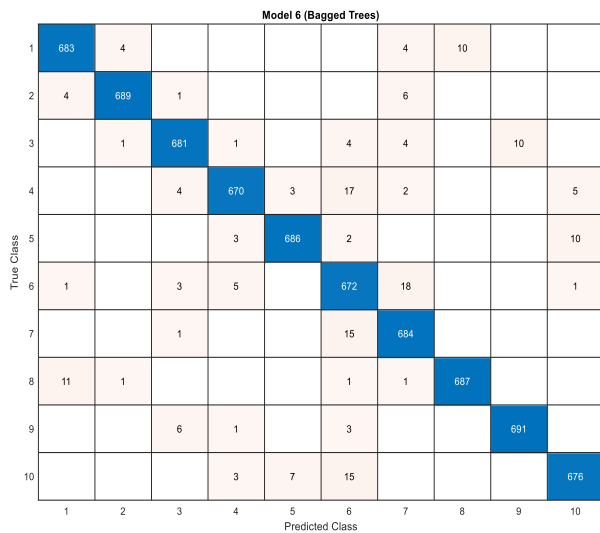


Figure 11. The confusion matrix for the Bagged Tree classifier during the training and testing phases.

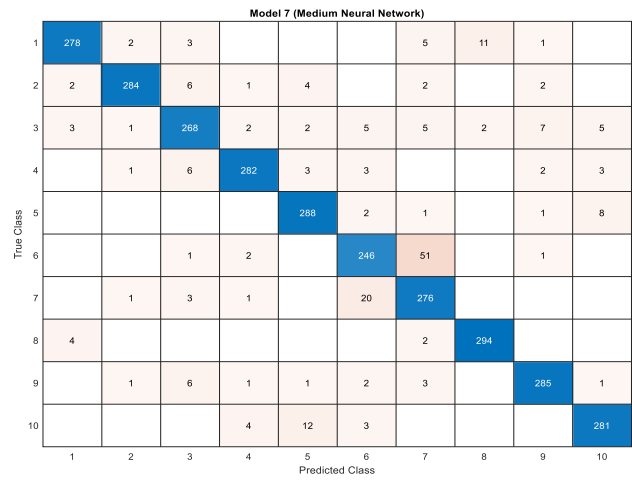
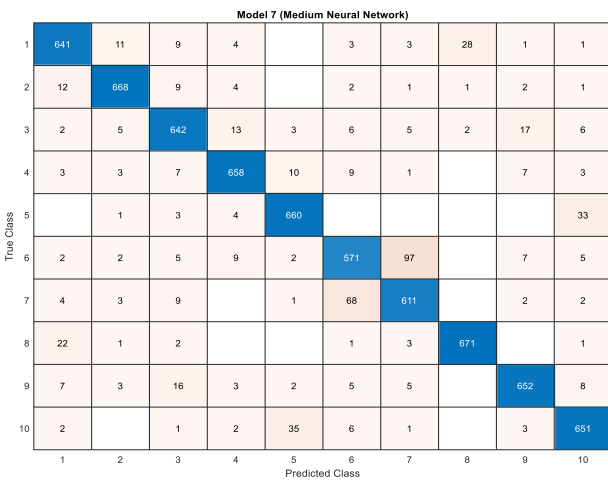


Figure 12. The confusion matrix for the ANN classifier during the training and testing phases.

Table.1 All dataset specification and classification model accuracies and times

Training Data Observations= 7007,			
Predictors: 48 features, Response: 49			
Response Classes: 10, Validation: 10-CV			
Testing Data Observations= 3003			
Model Type	Accuracy % (Train)	Accuracy % (Test)	Training Time (s)
KNN	98.916	98.169	14.05123
BT	97.317	97.269	163.939
QDA	93.435	93.173	3.941
ANN	92.641	91.694	216.666
DT	86.943	86.147	9.876
SVM	81.851	80.277	76.321
NB	80.386	79.849	408.607

Firstly, the confusion matrices indicate that the ML methods can predict both true positives and negatives well across all the observations (7007 for training and 3003 for testing), enhancing their predictive power. Secondly, the models capture the complexity and non-linearity of the relationships within the data well. Additionally, the 10-fold cross-validation strategy employed further ensures that the models are robust and less prone to overfitting, as they are tested on diverse subsets of the data. Finally, using 48 carefully selected features allows for effective representation of the underlying patterns within the data, leading to improved classification performance.

Figs. 13 and 14 depict the training and testing accuracies for all model classifiers and times.

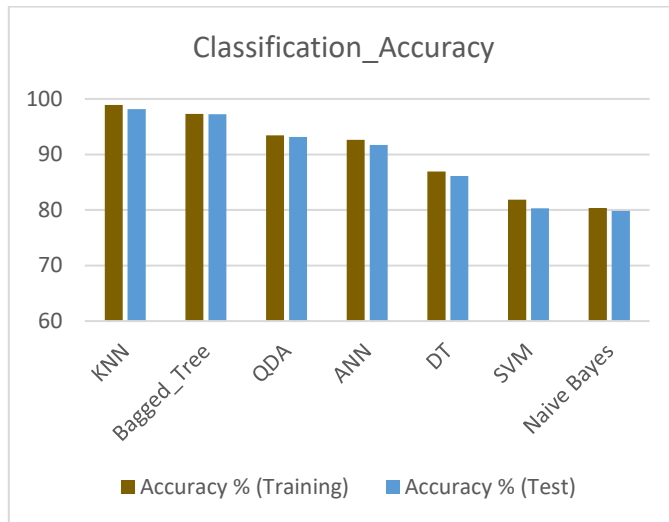


Figure 13. Training and testing accuracies for all classifiers

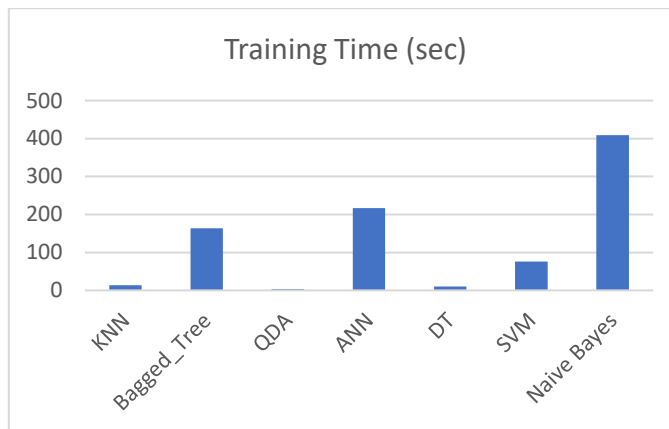


Figure 14. Training times for all classifiers

The accompanying table and figures provide the following thorough comparison: BT shows remarkable accuracy of 97.32% and 97.27%, respectively. KNN performs well, with 98.92% accuracy on the training set and 98.17% on the test set. The models' training times differ noticeably from one another. The two that take the longest, ANN and NB, are 216.67 and 408.61 seconds, respectively. On the other hand, time-efficient methods are DT and QDA. The best model for a classification task depends on the application's needs, data, and computational resources. For efficiency, choose QDA or DT. For high accuracy and abundant resources, consider KNN or BT.

6. Conclusion

Integrating GPR data as geophysical sources with efficient classification methods will provide a more comprehensive understanding of subsurface conditions, facilitating more informed decision-making in resource management. This work aims to enhance subsurface characterization of GPR data processing for real hydrocarbon oil and gas fields using advanced machine learning approaches: DT, BT, ANN, KNN, QDA, SVM, and NB, and to classify subsurface materials

effectively. Our results indicate that all models demonstrated commendable performance, with the KNN achieving the highest accuracy of 98.169%. This remarkable accuracy not only underscores the potential of machine learning in GPR data analysis but also emphasizes the effectiveness of our preprocessing techniques, which included feature extraction through Gray-Level Co-Occurrence Matrix (GLCM) and Wavelet transforms, as well as robust data normalization and missing value imputation.

In future work, exploring ensemble methods may lead to even greater accuracy and robustness by combining the strengths of multiple algorithms. Additionally, integrating deep learning approaches could enhance our ability to model complex subsurface structures and patterns. It is also recommended that data augmentation techniques be implemented to support model performance in scenarios with limited training data.

Acknowledgments

This work was supported by the Ministry of Higher Education and Scientific Research, Mustansiriyah University, Baghdad,

Iraq.

Conflict of interest

The authors declare that there are no conflicts of interest regarding the publication of this manuscript.

Author Contribution Statement

Mohanad Abd Shehab proposed the research problem, performed the methodologies and their computations, discussed the results, and revised the final manuscript.

Musab T.S. Al-Kaltakchi collected the datasets and revised the final manuscript.

Ammar Dukhan and Wai Lok Woo developed the methodologies and discussed the final results.

References

- [1] S. Wang, G. Liu, G. Jing, Q. Feng, H. Liu, and Y. Guo, "State-of-the-Art Review of Ground Penetrating Radar (GPR) Applications for Railway Ballast Inspection," *Sensors*, vol. 22, no. 7, p. 2450, Mar. 2022, doi: <https://doi.org/10.3390/s22072450>.
- [2] F. Sengani, "The use of ground Penetrating Radar to distinguish between seismic and non-seismic hazards in hard rock mining," *Tunnelling and Underground Space Technology*, vol. 103, p. 103470, Sep. 2020, doi: <https://doi.org/10.1016/j.tust.2020.103470>.
- [3] M. A. Shehab, M. Abdulridha Sahib Al Obaidi, I. Hos, and S. Karamzadeh, "Subspace Clutter Removal Techniques In Gpr Images," *Progress In Electromagnetics Research M*, vol. 82, pp. 139–147, 2019, doi: <https://doi.org/10.2528/pierm19032511>.
- [4] P. Senthil, A. Varughese, H. Dev, and S. L. Gupta, "Applications of Ground Penetrating Radar—A Comprehensive Case Study," *Lecture notes in civil engineering*, pp. 31–41, Jan. 2021, doi: https://doi.org/10.1007/978-981-16-1303-6_3.
- [5] X. Meng et al., "Ground-penetrating radar measurements of subsurface structures of lacustrine sediments in the Qaidam Basin (NW China): Possible implications for future in-situ radar experiments on Mars," *Icarus*

- (New York, N.Y. 1962), vol. 338, pp. 113576–113576, Mar. 2020, <https://doi.org/10.1016/j.icarus.2019.113576>.
- [6] S. A. Tabana, H. O. Ş. Ilknur, M. A. Shehab, and S. Karamzadeh, "Ground-Penetration Radar Signal Processing For Water Detection". *International Journal of Electronics Mechanical and Mechatronics Engineering*, 9(4), 2019, 1735-1750, https://scholar.google.com/scholar?hl=ar&as_sdt=0%2C5&q=Ground-Penetration+Radar+Signal+Processing+For+Water+Detection&btnG=
- [7] P. B. Rad and C. J. Hickey, "Using common-reflection-surface stack for enhanced near-surface seismic reflection imaging: Examples from consolidated and unconsolidated environments," *Geophysics*, vol. 87, no. 5, pp. EN45–EN56, Jul. 2022, <https://doi.org/10.1190/geo2021-0437.1>.
- [8] J. Ford and A. Camerlenghi, "Geostatistical characterization of the internal structure of mass-transport deposits from seismic reflection images and borehole logs," *Geophysical Journal International* (Print), vol. 221, no. 1, pp. 318–333, Dec. 2019, <https://doi.org/10.1093/gji/ggz570>.
- [9] J. Wang, H. Liu, P. Jiang, Z. Wang, Q. Sui, and F. Zhang, "GPRI2Net: A Deep-Neural-Network-Based Ground Penetrating Radar Data Inversion and Object Identification Framework for Consecutive and Long Survey Lines," *IEEE transactions on geoscience and remote sensing*, vol. 60, pp. 1–20, Jan. 2022, <https://doi.org/10.1109/tgrs.2021.3111445>.
- [10] S. Arrowsmith, D. Trugman, J. MacCarthy, K. Bergen, D. Lumley, and M. Magnani, "Big Data Seismology," *Reviews of Geophysics*, vol. 60, Jun. 2022, <https://doi.org/10.1029/2021RG000769>.
- [11] Z. Mao et al., "The relationship between crosslinking structure and silk fibroin scaffold performance for soft tissue engineering," *International Journal of biological macromolecules*, vol. 182, pp. 1268–1277, Jul. 2021, <https://doi.org/10.1016/j.ijbiomac.2021.05.058>.
- [12] A. Klotzsche, F. Jonard, M. C. Looms, J. van der Kruk, and J. A. Huisman, "Measuring Soil Water Content with Ground Penetrating Radar: A Decade of Progress," *Vadose Zone Journal*, vol. 17, no. 1, p. 180052, 2018, <https://doi.org/10.2136/vzj2018.03.0052>.
- [13] Iraklis Giannakis, A. Giannopoulos, and C. Warren, "A Machine Learning-Based Fast-Forward Solver for Ground Penetrating Radar With Application to Full-Waveform Inversion," *IEEE Transactions on Geoscience and Remote Sensing*, vol. 57, no. 7, pp. 4417–4426, Jul. 2019, <https://doi.org/10.1109/tgrs.2019.2891206>.
- [14] I. Giannakis, A. Giannopoulos, and C. Warren, "A Machine Learning Scheme for Estimating the Diameter of Reinforcing Bars Using Ground Penetrating Radar," *IEEE Geoscience and Remote Sensing Letters*, pp. 1–5, 2020, <https://doi.org/10.1109/lgrs.2020.2977505>.
- [15] H. Liu, C. Lin, J. Cui, L. Fan, X. Xie, and B. F. Spencer, "Detection and localization of rebar in concrete by deep learning using ground penetrating radar," *Automation in Construction*, vol. 118, p. 103279, Oct. 2020, <https://doi.org/10.1016/j.autcon.2020.103279>.
- [16] N. Smitha and V. Singh, "Target detection using supervised machine learning algorithms for GPR data," *Sensing and Imaging*, vol. 21, no. 1, Feb. 2020, <https://doi.org/10.1007/s11220-020-0273-8>.
- [17] Z. Xiang, G. Ou, and A. Rashidi, "Automated Translation of Rebar Information from GPR Data into As-Built BIM: A Deep Learning-based Approach," *arXiv (Cornell University)*, Oct. 2021, <https://doi.org/10.48550/arxiv.2110.15448>.
- [18] L. C. M. Amaral, A. Roshan, and A. Bayat, "Review of Machine Learning Algorithms for Automatic Detection of Underground Objects in GPR Images," *Journal of Pipeline Systems Engineering and Practice*, vol. 13, no. 2, May 2022, [https://doi.org/10.1061/\(asce\)ps.1949-1204.0000632](https://doi.org/10.1061/(asce)ps.1949-1204.0000632).
- [19] M. Rasol et al., "GPR monitoring for road transport infrastructure: A systematic review and machine learning insights," *Construction and Building Materials*, vol. 324, p. 126686, Mar. 2022, <https://doi.org/10.1016/j.conbuildmat.2022.126686>.
- [20] G. Roncoroni, E. Forte, L. Bortolussi, and M. Pipan, "Efficient extraction of seismic reflection with Deep Learning," *Computers & Geosciences*, vol. 166, p. 105190, Sep. 2022, <https://doi.org/10.1016/j.cageo.2022.105190>.
- [21] A. Bauer, J. Walda, and D. Gajewski, "Transfer learning seismic and GPR diffraction separation with a convolutional neural network," Aug. 2022, <https://doi.org/10.1190/image2022-3749913.1>.
- [22] D. C. Bowden. *The propagation and amplification of surface waves*, California Institute of Technology, 2018, <https://doi.org/10.7907/Z9DR2SPR>.
- [23] S. AL-khyat, D. Naji, H. T. Hamad, and H. Onyeaka, "A Review On Soil Contamination Sources: Impact On Engineering Properties And Remediation Techniques," *Journal of Engineering and Sustainable Development*, vol. 27, no. 3, pp. 292–307, May 2023, <https://doi.org/10.31272/jeasd.27.3.1>.
- [24] H. Sahoo, M. Royhan Gani, G. J. Hampson, N. D. Gani, and A. Ranson, "Facies- to sandbody-scale heterogeneity in a tight-gas fluvial reservoir analog: Blackhawk Formation, Wasatch Plateau, Utah, USA," *Marine and Petroleum Geology*, vol. 78, pp. 48–69, Dec. 2016, <https://doi.org/10.1016/j.marpetgeo.2016.02.005>.
- [25] S. U. Eze, D. O. Ogarue, S. L. Nnorom, W. E. Osung, and T. A. Ibitoye, "Integrated geophysical and geochemical methods for environmental assessment of subsurface hydrocarbon contamination," *Environmental monitoring and assessment*, vol. 193, no. 7, Jun. 2021, <https://doi.org/10.1007/s10661-021-09219-3>.
- [26] N. H. El-Gendy, A. E. Radwan, M. A. Waziry, Thomas J.H. Dodd, and Moataz Kh Barakat, "An integrated sedimentological, rock typing, image logs, and artificial neural networks analysis for reservoir quality assessment of the heterogeneous fluvial-deltaic Messinian Abu Madi reservoirs, Salma field, onshore East Nile Delta, Egypt," *Marine and petroleum geology*, vol. 145, pp. 105910–105910, Nov. 2022, <https://doi.org/10.1016/j.marpetgeo.2022.105910>.
- [27] K. M. Fouad, M. M. Ismail, A. T. Azar, and M. M. Arafa, "Advanced methods for missing values imputation based on similarity learning," *PeerJ Computer Science*, vol. 7, p. e619, Jul. 2021, <https://doi.org/10.7717/peerj-cs.619>.
- [28] M. A. Shehab and N. Kahraman, "A weighted voting ensemble of efficient regularized extreme learning machine," *Computers & Electrical Engineering*, vol. 85, p. 106639, Jul. 2020, <https://doi.org/10.1016/j.compeleceng.2020.106639>.
- [29] P. Soltani, A. R. Kahoo, and H. Hasanpour, "Proposing new seismic texture attributes based on novel gray level matrix with application to salt dome detection," *Journal of Applied Geophysics*, vol. 218, p. 105214, 2023. <https://doi.org/10.1016/j.jappgeo.2023.105214>.
- [30] A. Ali, C. Sheng-Chang, and M. Shah, "Continuous wavelet transformation of seismic data for feature extraction." *SN Applied Sciences*, vol. 2, pp. 1-12, 2020. <https://doi.org/10.1007/s42452-020-03618-w>.